

Probing thermal magnon current via nitrogen-vacancy centers in diamond

Dwi Prananto^{1*†}, Yuta Kainuma¹, Kunitaka Hayashi¹, Norikazu Mizuochi²,

Ken-ichi Uchida^{3,4,5}, Toshu An^{1‡}

¹*School of Materials Science, Japan Advanced Institute of Science and Technology,*

Nomi, Ishikawa 923-1292, Japan

²*Institute for Chemical Research, Kyoto University, Gokasho, Uji, Kyoto 611-0011,*

Japan

³*National Institute for Materials Science, Tsukuba 305-0047, Japan*

⁴*Institute for Materials Research, Tohoku University, Sendai 980-8577, Japan*

⁵*Center for Spintronics Research Network, Tohoku University, Sendai 980-8577, Japan*

*e-mail: prananto@jaist.ac.jp

† Present address: Materials Science Program, Faculty of Engineering, Niigata University, Niigata City, Niigata 950-2181, Japan

‡e-mail: toshuan@jaist.ac.jp

Currently, thermally excited magnons are being intensively investigated owing to their potential in computing devices and thermoelectric conversion technologies. We report the detection of thermal magnon current propagating in a magnetic insulator yttrium iron garnet under a temperature gradient, using electron spins associated with nitrogen-vacancy (NV) centers in diamond. By exploiting the interplay between coherent and incoherent magnons, thermal magnon current is observed via NV spins hosted in a beam-shaped bulk diamond and a nanodiamond coupled with coherent magnon in the form of modified Rabi oscillation frequencies as well as spin relaxation rates. The local probing of thermal magnon current serves as a basis for creating a new device platform hybridizing spin caloritronics and spin qubits.

Introduction

The utilization of magnons, i.e., the quanta of collective excitation of spins, in a magnetically ordered media for transmitting and processing information has flourished in the recent decade and is known as magnon spintronics¹⁻⁴. Moreover, the emerging field of spin caloritronics⁵, which utilizes the interplay between spin and heat currents, resulted in an alternative strategy in creating more efficient computing devices^{6,7} and

versatile thermoelectric conversion technologies⁸. The advancement of this field relies on the ability to sensitively probe spin dynamics without distracting the system.

Quantum sensors based on the electron spins associated with nitrogen-vacancy (NV) centers in diamond^{9,10} has been regarded as high-resolution and high-sensitivity sensors for various condensed matter phenomena¹¹. NV centers can be strongly coupled with coherent magnetostatic spin waves (MSWs) owing to their energy matching (one to tens of gigahertz)¹²⁻¹⁸. Thermally excited magnons, which appear in a significantly higher energy regime (defined by $\hbar\omega = k_B T$) than NV spins, are rarely investigated through NV spin-based magnetometry owing to the gap between their energies. These incoherent and high energy magnons are known to interact with lower-energy magnons MSWs by transferring their spin angular momentum, known as the thermal magnon spin-transfer torque¹⁹⁻²⁴.

Recently, magnon population has been measured and controlled via pumping the NV center by spin waves at the NV spin resonance frequencies with a single NV spin sensitivity²⁵⁻²⁷. Furthermore, the same effect was observed nonlocally using the inverse spin Hall effect²⁸. Additionally, NV spin excitations and modulations via the spin-

transfer-torque oscillation of spin waves by electrical methods through the spin Hall effect has been demonstrated recently^{29,30}.

Herein, we report the detection of thermally excited magnon current by exploiting the thermal magnon spin-transfer torque. Using the NV spins hosted in a bulk single crystal and a nanocrystal diamond, we observed the modification of the MSWs' magnetization dynamics under the effect of the thermal magnon current applied to a magnetic insulator yttrium iron garnet (YIG) sample.

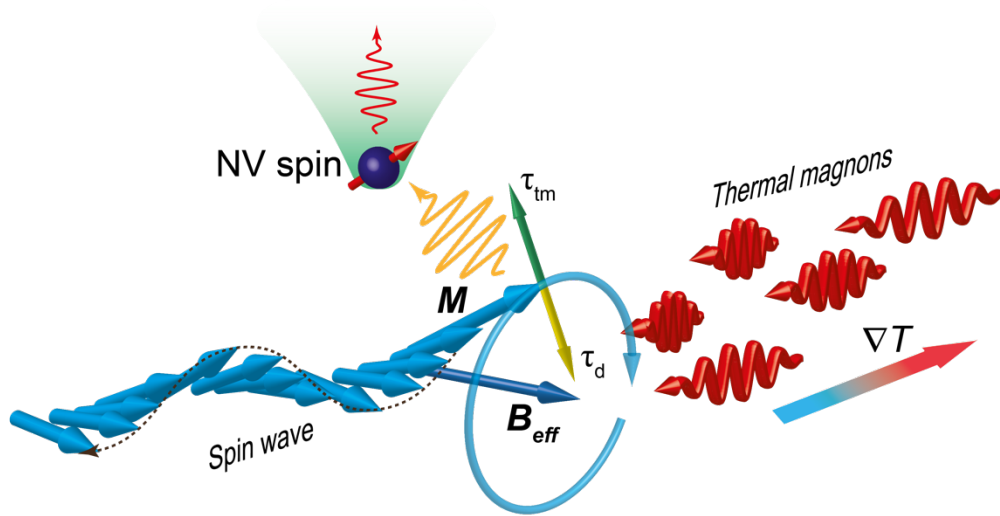


Figure 1| Mechanism of thermal magnon current detection. *Nitrogen-vacancy center spin in diamond probes thermally excited magnon current mediated by magnetostatic spin waves.*

Results

System and experimental procedure

We used a trilayer of single-crystalline YIG/gadolinium gallium garnet (GGG)/YIG of thicknesses 100, 550, and 100 μm , respectively, measuring 6 mm \times 3 mm (Fig. 2a). To improve the lattice matching between YIG and GGG, a small amount of Y in YIG was substituted with Bi. An in-plane external magnetic field was applied along the y-axis, colinear with two gold-wires antenna (50 μm in diameter) placed on both edges of the YIG.

We used two types of diamond to host the NV centers as a quantum sensor for the detection of thermally excited magnons; a diamond beam ((110) oriented) measuring 2.5 mm \times 0.1 mm \times 0.1 mm containing a layer of the NV spin ensemble and a nanocrystal diamond of diameter approximately 40 nm containing several NV spins. An in-plane external magnetic field directed along the y-axis created an angle of approximately 31.75° to the $[00\bar{1}]$ direction (23° to NV1 ($[\bar{1}\bar{1}\bar{1}]$)) in the diamond beam (Fig. 2a). Both the diamond beam and the nanodiamond were placed in the middle of the YIG's longitudinal direction.

A temperature gradient was created along the longitudinal direction in the YIG sample by increasing or lowering the temperature at either site A (T_A) or site B (T_B) (Fig. 2a). Using the temperature sensing capability of the NV spins^{31,32} and owing to the high thermal conductivity of diamond, the temperature in the middle of the YIG's longitudinal dimension was observed to be constant under the application of temperature difference ΔT up to 10 K (see Supplementary Information). ΔT is defined as the difference between T_A and T_B ($\Delta T = T_A - T_B$).

We used the NV spins' ground triplet (3A_2) states, $m_s = 0$ and $m_s = \pm 1$, optically addressed using an in-house scanning confocal microscope. The spin-state selective photoluminescence (PL) nature of the NV spin allows us to optically discriminate the spin qubit states ($m_s = 0$ yields a higher PL than $m_s = \pm 1$). Spin-state manipulation, $m_s = 0 \leftrightarrow \pm 1$ was performed by the MSW-generated microwave radiation excited from the gold-wire antennas separated approximately 2 mm away from the laser spot position. This coherent magnons propagating along the $\mathbf{k} \parallel \mathbf{B}_{\text{ext}} \times \hat{\mathbf{n}}$ direction ($\hat{\mathbf{n}}$ is vector normal to the YIG's surface), is typically known as magnetostatic surface spin waves (MSSWs)³³.

Spin wave and NV spin resonance mapping

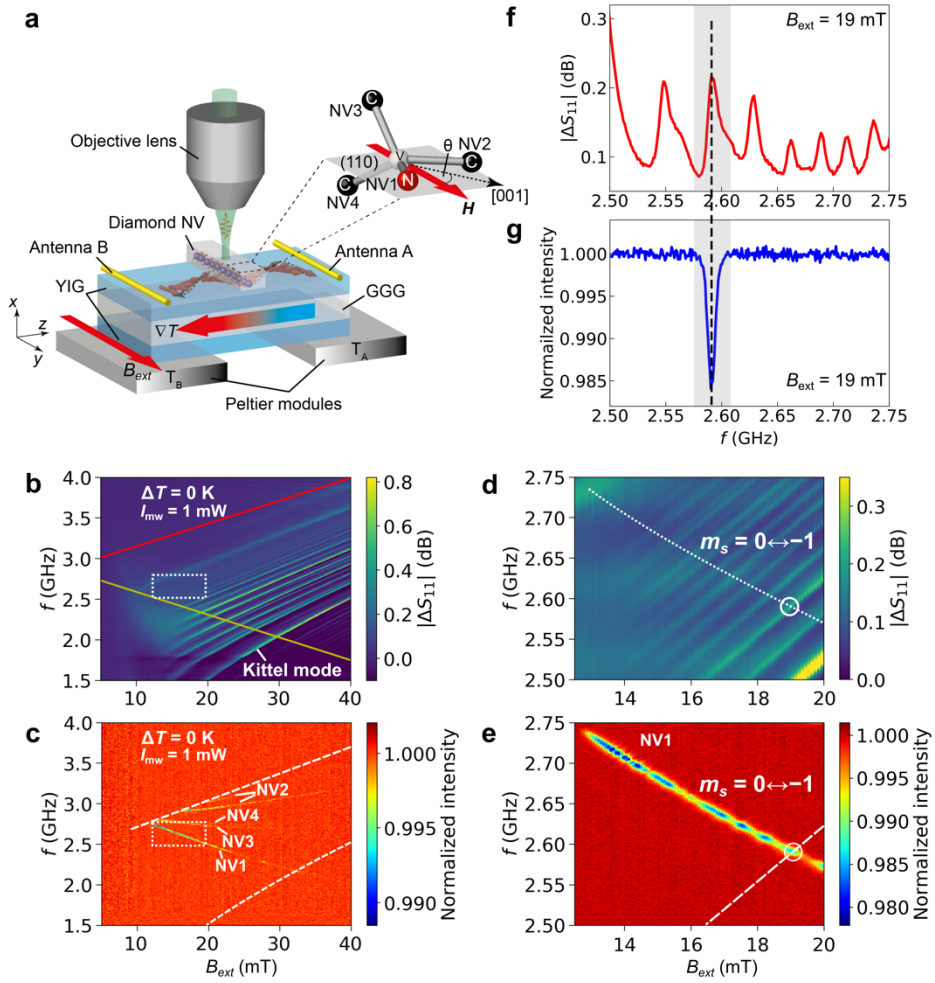


Figure 2| Experimental setup and mapping of spin waves and NV spin resonances.

a, Experimental setup for probing thermally excited magnon current via NV centers in diamond beam. *b*, Microwave-reflected spin wave resonance spectra as a function of externally applied magnetic field. Solid lines indicate upper (red, $m_s = 0 \leftrightarrow +1$) and lower (yellow, $m_s = 0 \leftrightarrow -1$) bounds of possible ground state resonance transition of NV spins. *c*, ODMR spectra of the NV spins in diamond beam as a function of externally

applied magnetic field B_{ext} . The region between the two dashed white lines indicate the resonance frequency band of magnetostatic surface spin waves. NV1 to NV4 indicate four possible NV spins directed to $\langle 111 \rangle$ symmetrical axes, as shown in **a**. **d**, Zoomed spin wave resonance spectra at dotted white square in **b**. Dashed white line indicates resonance transitions of NV spins in **c**. **e**, Zoomed ODMR spectra in dotted white square in **c**, showing discretized ODMR resonance line of NV1 owing to crossing with MSSWs' resonant frequencies. **f**, Line cut of **d** at $B_{ext} = 19$ mT. **g**, Line cut of **e** at $B_{ext} = 19$ mT. Both **f** and **g** show matching condition at frequency 2.59 GHz.

First, we mapped out the YIG's global coherent spin-waves resonance spectra by performing microwave reflection (S_{11} -parameter) measurement using a vector network analyzer (Rohde & Schwartz ZVB8) at zero temperature difference. Figure 2b shows a map of the spin-wave spectra in an increasing external magnetic field B_{ext} , exhibiting lines of resonance spanning from the uniform Kittel mode (ferromagnetic resonance) at the bottom line to the MSSWs with the highest wave vector k at the upper-most line. The solid red and yellow lines indicate the NV spins' upper ($m_s = 0 \leftrightarrow +1$) and lower ($m_s = 0 \leftrightarrow -1$) bound resonance transitions defined by the Zeeman energy, respectively. As demonstrated by Kikuchi et al.¹⁶ and Andrich et al.¹⁵, when a matching

condition between the MSSW and NV spins is fulfilled ($f_{\text{MSSW}} = f_{\text{NV}}$), the NV spins can be coherently excited by the MSSW. From the result in Fig. 2b, we can expect excitations of NV spins by the MSSWs within the frequencies spanning between the red and yellow lines.

Next, we mapped out the MSSW-driven NV spins resonance frequencies by performing optically detected magnetic resonance (ODMR) spectroscopy with an increasing external magnetic field B_{ext} at zero temperature difference. Figure 2c shows a color map of the MSSW-driven electron spin resonance from an ensemble of NV spins in the diamond beam. As expected, only the NV spins' resonance transitions that matched with the MSSW's resonance frequencies underwent PL intensity quenching as a consequence of the transition from $m_s = 0$ to $m_s = \pm 1$. In Fig. 2c, only the $m_s = 0 \leftrightarrow -1$ transitions that overlapped with the MSSW's resonance frequencies resulted in vanishing resonance lines for $m_s = 0 \leftrightarrow +1$ transitions. Furthermore, by zooming in around the NV1 spectral line in Fig. 2c, a discretized and broadened resonance line owing to the frequency matching between the NV spins and the different MSSW modes (Fig. 2d) was observed^{17,34} (Fig. 2e). The matching condition between one of the MSSW modes and the NV spins is shown in Figs. 2f and g.

Detection of thermal magnon current via coherent driving of NV spins

Using an ensemble of NV spins in the diamond beam, the ODMR spectra of the NV spins were first analyzed under a temperature gradient to detect thermal magnon flow via a coherent alternating current (AC) magnetic field generated by the MSSW. We tuned the resonance frequency to one of the matching condition frequencies of 2.58 GHz and analyzed the PL contrast of the ODMR as the temperature difference ΔT varied. In Figure 3a, the ODMR spectra with resonance dips at 2.58 GHz are shown with increasing ΔT . The ODMR's PL contrast enhanced as ΔT evolved from positive to negative, indicating a change in the MW excitation power from that of the MSSWs³⁵. Hence, the linear dependence of PL contrast on ΔT (see Fig. 3b) is an implication of the change in MW excitation strength by the MSSW as thermal magnon current was generated under the application of temperature gradient in the YIG.

Next, the NV spins were driven into their Rabi oscillations between the qubit states of $m_s = 0$ and $m_s = -1$. The frequency of the Rabi oscillation Ω_R is proportional to the square root of the oscillation's driving strength $\Omega_R \propto \sqrt{P_{MW}}$ ³⁶ and hence can be used to detect the change in the MSSW's magnetization dynamics that drives the Rabi oscillation^{15,16}. We drove the Rabi oscillation via the MSSW launched from antenna A,

tuned to the matching condition of 2.58 GHz and simultaneously applying a temperature gradient to the YIG. In this case, the applied external magnetic field is assigned as $+B_{\text{ext}}$ as it is colinear with the $+y$ axis. The Rabi frequency enhanced as ΔT progressed from 0 to -10 K and diminished as ΔT progressed from 0 to $+10$ K (Figs. 3c and d, respectively). The Rabi field can be estimated from the Rabi frequency through the relation $b_R = \Omega_R/\gamma_e$ ^{12,36,37}, with $\gamma_e = 2\pi \cdot 28$ GHz/T being the gyromagnetic ratio of electrons. The Rabi field b_R evolved from 18 μT at $\Delta T = 10$ K to 26 μT at $\Delta T = -10$ K, based on its plot as a function of temperature difference (Fig. 3e); this indicates a change of approximately 18% from zero temperature difference.

MSSWs are widely known to propagate unidirectionally and in opposite directions at each surface in a ferromagnetic medium^{38,39}. Hence, we can expect to observe the same effect with an inverted sign when we switch the external magnetic field to the $-y$ axis ($-B_{\text{ext}}$) and launch the MSSWs from antenna B²⁴. We tuned the NV resonance frequency to a matching condition of 2.60 GHz. As expected, we observed an enhancement in the Rabi frequency as the temperature difference increased to the positive regime from zero temperature difference and a suppression as the temperature

difference increased to the negative regime from zero temperature difference (Figs. 3f and g). In this geometry, the Rabi field is estimated to evolve from approximately 18 μT at $\Delta T = -10$ K to approximately 22 μT at $\Delta T = 10$ K (Fig. 3h).

The observed effect can be interpreted as a thermal magnon spin-transfer torque via the thermal magnon current generated by a temperature gradient^{4,40,41}, which interacts with the MSSW and relaxes by transferring its spin angular momentum. The transfer of spin angular momentum contributes to the development of an anti-damping torque τ_{tm} , which alters the MSSW's magnetization dynamics^{19,20,24} and perceived by the NV spins as an altering Rabi field strength (see Fig. 1a). The effect can be described phenomenologically by the Landau–Lifshitz–Gilbert (LLG) equation of magnetization dynamics with an additional term from the anti-damping torque induced by the thermal magnon current, as follows:²⁴

$$\frac{d\mathbf{M}}{dt} = \gamma_e(\mathbf{M} \times \mathbf{B}_{\text{eff}}) + \frac{\alpha_i}{M_s} \left(\mathbf{M} \times \frac{d\mathbf{M}}{dt} \right) + \gamma_e \boldsymbol{\tau}_{tm}, \quad (1)$$

where \mathbf{M} is the magnetization of YIG, \mathbf{B}_{eff} the effective excitation AC magnetic field responsible for the magnetization precession, α_i the intrinsic Gilbert damping parameter of the magnetization dynamics, M_s the saturation magnetization, and $\boldsymbol{\tau}_{tm}$ the anti-damping torque induced by the thermal magnon current defined by²⁴

$$\boldsymbol{\tau}_{tm} = \alpha_{tm} \frac{\omega}{|\gamma_e| M_s^2} \mathbf{M} \times (\mathbf{M} \times \mathbf{m}). \quad (2)$$

α_{tm} , ω , and \mathbf{m} are the thermal magnon torque damping parameter, resonance frequency, and non-equilibrium component of magnetization, respectively.

Figure 4 shows a schematic of a toy model for analyzing the phenomenon and inferring the thermal magnon torque damping parameter from the observed effect. From the toy model in Fig. 4, the effective field of the system is expressed as $\mathbf{B}_{\text{eff}} = \mathbf{B}_{\text{ext}} + \mathbf{b}_R + \mathbf{B}_d$, where \mathbf{B}_{ext} and \mathbf{b}_R are the external and Rabi fields, respectively, and \mathbf{B}_d is the demagnetization field that equals to $-\mu_0 \mathbf{M}_{\text{eff}}$. This effective field produces an effective magnetization in the YIG, expressed as $\mathbf{M}_{\text{eff}} = \mathbf{M}_s + \mathbf{m}$, where \mathbf{M}_s ($\mu_0 M_s = 11.9$ mT for the YIG used in the experiment) is the saturation magnetization, and \mathbf{m} is transverse component of the magnetization precession. As the precession cone angle of a magnetostatic spin wave is small ($< 1^\circ$)⁴², the effective magnetization can be simplified as $\mathbf{M}_{\text{eff}} \approx \mathbf{M}_s$.

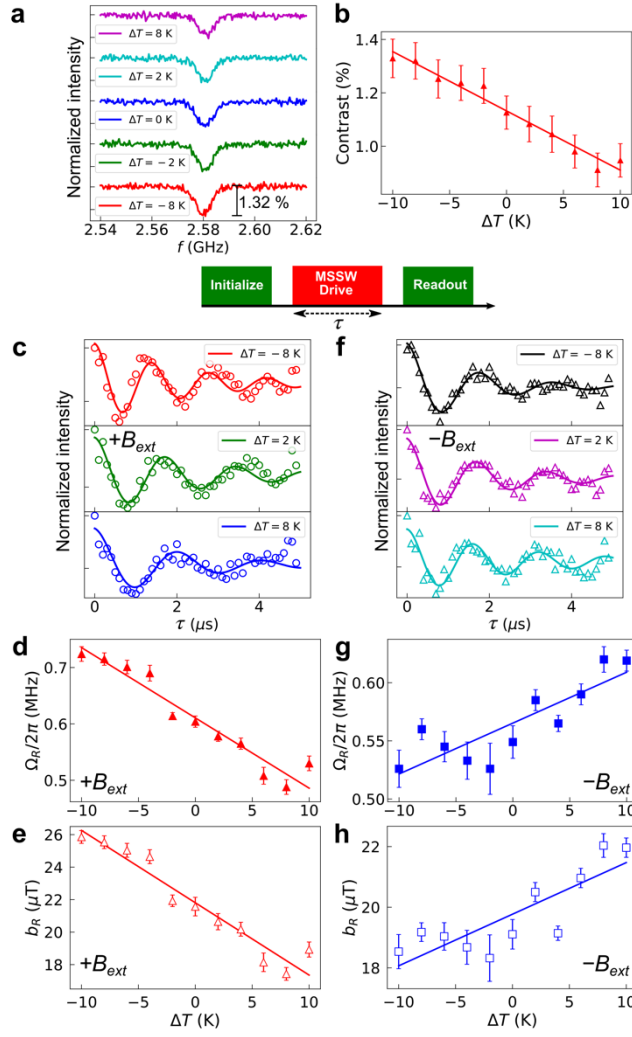


Figure 3| ODMR spectra and Rabi oscillation frequency as a function of temperature difference. *a*, ODMR spectra with various temperature differences ΔT applied to the YIG at $B_{ext} = 19.4$ mT. Resonance dip contrast evolved with temperature difference ΔT applied to the YIG. *b*, ODMR contrast as a function of temperature difference ΔT applied to the YIG. *c*, Rabi oscillation at three different temperature differences ΔT applied to the YIG for positive external magnetic field

$B_{ext} = +19.4$ mT. Frequency of Rabi oscillation evolved with applied temperature difference. Rabi oscillation measurement protocol (depicted on top) comprises two laser pulses to initialize and readout NV spin state and an MW pulse with variable pulse width τ at a frequency that matched both MSSW and NV Spins. **d**, Variation in Rabi oscillation frequency $\Omega_R/2\pi$ with temperature difference. **e**, Calculated Rabi field b_R inferred from Rabi frequency in **d** as a function of applied temperature difference ΔT . **f-h**, Rabi oscillations, Rabi frequencies, and Rabi fields, respectively as a function of temperature difference with negative applied external magnetic field of $B_{ext} = -19$ mT.

Under the resonance condition, the magnetic damping parameter can be expressed in terms of the imaginary part of the dynamic susceptibility as follows:⁴³

$$\chi_r'' = \frac{\omega_M}{2\alpha_{eff}\omega_r}, \quad (3)$$

where ω_r is the spin wave resonance angular frequency, $\omega_M = -\gamma_e\mu_0 M_s$, and $\alpha_{eff} = \alpha_i + \alpha_{tm}$ is the effective damping parameter defined by the sum of the intrinsic Gilbert damping parameter α_i of the YIG and the damping parameter from the thermal magnon α_{tm} .

Because our measurement of the Rabi oscillation as a function of temperature difference was performed under a matching condition, we can infer a relation between the Rabi field b_R and the damping parameter α_{eff} as $b_R = -\alpha_{\text{eff}}\omega_r/2\pi\gamma_e - B_{\text{ext}} + \mu_0 M_s$. As α_{tm} evolves with the temperature gradient ($\alpha_{\text{tm}} = a\nabla T$), the Rabi field can be expressed in terms of the temperature gradient as follows:

$$b_R = -\alpha_i \frac{\omega_r}{2\pi\gamma_e} - a \frac{\omega_r}{2\pi\gamma_e} \nabla T - B_{\text{ext}} + \mu_0 M_s. \quad (4)$$

From the slope of the Rabi field as a function of temperature difference (Figs. 3e and h), a proportionality constant a can be obtained, and the thermal magnon damping parameter α_{tm} was estimated to be 0.3×10^{-4} for $+B_{\text{ext}}$ and 0.1×10^{-4} for $-B_{\text{ext}}$ at an effective temperature difference of $\Delta T_{\text{eff}} = 5.6$ K at the YIG surface. We used $\nabla T_{\text{eff}} = 5.6$ K/mm for ∇T since the MSSWs propagated on the surface from an antenna to the center position, and the effect occurred within the half of the YIG's longitudinal direction. These damping parameter values from thermal magnon torque agreed well with those reported previously²¹⁻²⁴, confirming the existence and contribution of thermal magnon current in the evolution of MSSW magnetization dynamics^{19,20,24}.

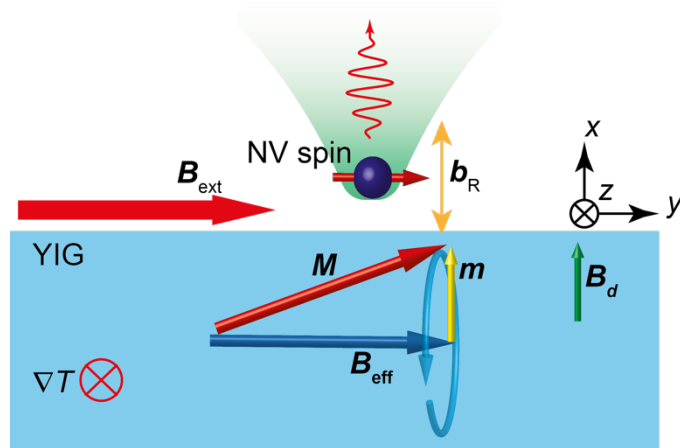


Figure 4| Analytical model of the observed phenomenon. *A toy model of thermal magnon current spin-transfer torque system with a NV spin (blue ball with red arrow) and a precessing magnetization \mathbf{M} in YIG (red arrow). The precessing magnetization produces an AC magnetic field (\mathbf{b}_R) that drives the NV spin into its Rabi oscillation.*

Local detection via non-resonant NV spin excitation

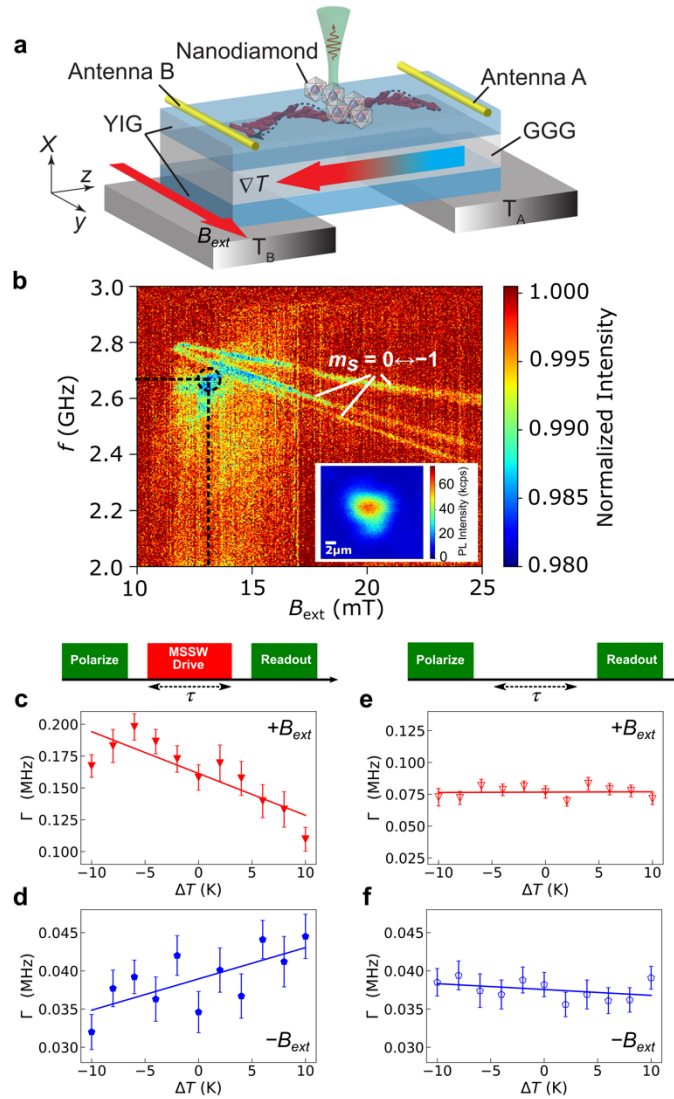


Figure 5| Experimental setup and results of local detection of thermal magnon

current. **a**, *Experimental setup for local detection of the thermally excited magnon current. Diamond beam was replaced with a nanocrystal of diamond with several NV spins.* **b**, *ODMR spectra map of NV spins in nanocrystal diamond on YIG under zero temperature difference. Non-resonant PL quenching was observed beside the straight*

lines of the NV spin transitions $m_s = 0 \leftrightarrow -1$. Inset shows a fluorescence map of the nanodiamond used in the measurement. **c**, Longitudinal spin relaxation rate measurement protocol to detect the thermally excited magnon current comprising a polarizing laser pulse followed by a variable duration- τ pulse of non-resonant NV spin excitation via MSSW at frequency 2.66 GHz; $+B_{ext}$ and $-B_{ext}$ were 13.1 mT (dashed black circle in **b**). NV spin relaxation rate Γ shows linear dependence to temperature difference ΔT applied to the YIG. Positive **c** and negative **d** external fields show opposite trends owing to the non-reciprocal nature of MSSWs. **e**, Measurement protocol for control experiment performed without MSSW driving pulse. NV spin relaxation rate Γ shows no dependence on temperature difference ΔT for both positive **e** and negative **f** external magnetic fields.

We extended the capability to detect the thermally excited magnon current locally via a small number of NV spins in a nanocrystal diamond (adamas nano). Using the same setup and technique as in the experiment involving the diamond beam, we mapped out the ODMR spectra of the NV spins in the nanodiamond to obtain information regarding the coupling between the MSSW and the NV spins. Figure 5b shows the MSSW-driven ODMR spectral map exhibiting PL quenching at the resonance transition ($m_s = 0 \leftrightarrow$

–1) of the NV spins. Additionally, a strong PL quenching was observed away from the NV spin transitions, at frequencies from 2.5 to 2.7 GHz at the B_{ext} between 11.5 and 13.5 mT.

The spin wave resonance spectra maps in Figs. 2b and d show a strong non-resonant PL quenching in the region where the MSSW with high k -wave vectors was observed.

This non-resonant excitation is expected to change the longitudinal relaxation rate of the optically polarized $m_s = 0$ state of the NV spins in the nanodiamond owing to its proximity to the surface of the YIG. Under a perturbing dipolar field from non-resonant MSSWs with a k -wave vector that matches the inverse of the distance separating the NV spins and the YIG surface, the longitudinal relaxation rate of the NV spins has been shown to improve, resulting in PL quenching^{12,25-27,44}. Recently, similar non-resonant effects were observed and attributed to PL quenching by parametric magnon excitation⁴⁵.

Based on the principle of the thermal magnon spin-transfer torque, we can expect the amplitude-modulation of the non-resonant MSSWs to alter the relaxation rate of the NV spins as a temperature gradient is applied to the YIG. We performed longitudinal spin relaxation spectroscopy, in which NV spins were polarized to $m_s = 0$ by laser,

followed by a dark time for duration τ before another laser was applied to read the remaining population. By varying τ , the time-trace relaxation of the $m_s = 0$ state to its equilibrium state was observed. The relaxation rate Γ can be inferred as the inverse of the time constant T_1 of the exponentially decaying population at $m_s = 0$. The MSSW at frequency 2.66 GHz and $+B_{\text{ext}}$ and $-B_{\text{ext}} = 13.1$ mT (marked by dashed black circle in Fig. 5b) was driven during time τ to perturb the relaxation process and apply the temperature gradient to the YIG. Figures 5c and d show the linear dependence of the relaxation rate Γ on the ΔT applied to the YIG for positive and negative external magnetic fields, respectively.

The relaxation rate Γ is proportional to the stray magnetic field noise generated by the MSSW, as described by $\Gamma \sim \frac{\gamma_e^2}{2} |B_{\perp}|^2$, with $|B_{\perp}|^2$ the fluctuating magnetic field noise perpendicular to the NV's quantum axis¹². According to the fluctuation-dissipation theorem, this fluctuating magnetic field noise is proportional to the imaginary part of the dynamic susceptibility χ'' of the magnet^{12,46} and hence is related to the effective damping parameter α_{eff} , as described in equation (3). From Figs. 5c and d, we can infer that the magnetic field noise from the MSSW evolved proportionally with the temperature difference, indicating that coupling occurred between the thermally excited

magnon current and the MSSW, thereby affecting the damping mechanism of the precessing magnetization owing to the spin angular momentum transfer between the two magnon species.

Additionally, we performed a control experiment in which spin relaxation spectroscopy was performed without driving an MSSW (Figs. 5e and f). The results in Figs. 5e and f show no dependence of spin relaxation rates on temperature difference (both graphs are plotted with the same y-axis scale as Figs. 5c and d, respectively). The results indicate that 1) the energy of the thermally excited magnons is beyond the detection capability of the NV spins; therefore, they cannot directly be detected by the NV spins. 2) The MSSW is important as a medium for the NV spins to detect thermally excited magnon currents.

Discussion

We demonstrated the detection of thermally excited magnon currents mediated by coherent magnons via NV spins, where the thermal magnon spin-transfer torque emanated from the thermal magnon current altered the magnetostatic spin-waves' magnetization precession when the YIG magnetic sample was subjected to a

temperature gradient. The modulation of the magnetization dynamics of the MSSWs was perceived by the NV spins through the alteration of the Rabi oscillation frequency with the resonant NV spin excitation using a beam-shaped bulk diamond as well as the longitudinal spin relaxation rate with the non-resonant NV spins excitation using a nanodiamond. It is noteworthy that the use of the diamond-beam with a known NV axis direction is suitable for efficient resonant NV spin excitations but not for non-resonant excitations owing to the significant distance of approximately 1 μm separating the NV spins and the YIG surface¹⁸. Meanwhile, the use of nanodiamonds with an unknown NV axis is not suitable for efficient resonant NV spin excitations but suitable for non-resonant excitations because of their proximity to the YIG surface⁴⁷.

This study provides a novel detection tool for thermal magnon currents via the NV center, which can be located locally and in a broad range of distances to spin waves.

This feature cannot be obtained if only conventional methods, such as electrical detection via the inverse spin Hall effect, is used to investigate magnon dynamics, as the conventional method requires a relatively large electrode and specific configurations with proximal distance to the spin waves. Owing to the NV spin's single spin detection sensitivity enabled by its atomic-scale size⁴⁸, nanoscale probing and imaging of magnon

dynamics can be realized in the future, which can provide insights into novel practical applications in spin caloritronics and magnon spintronics^{12,17,29}.

Furthermore, the observed effect demonstrated the control of the NV spin quantum state by thermal magnons, enabled by MSWs. This introduces the potential application of a novel hybrid quantum information processing system⁴⁹, where distant NV spins are bridged by a ferromagnet and can be coherently mediated and controlled via spin waves and thermal magnons to produce entanglements over long distances under ambient conditions^{15,16,30}.

Method

Diamond beam fabrication

We used a diamond with (110) crystal orientation fabricated via chemical vapor deposition by EDP Corporation. NV defects were created in the diamond by implanting ¹⁴N⁺ ions using the ion source facility at the Japan Advanced Institute of Science and Technology, Center for Nano Materials and Technology with an implantation energy of 30 keV and a dose of 1×10^{12} ions/cm². The implantation was followed by annealing at 900 °C for 2 h to mobilize the vacancies to pair with the

nitrogen atoms. Using Monte Carlo simulations with the stopping ranges of ions in matter software package⁵⁰, we estimated that the NV defects layer was distributed at the depth of approximately 33 nm beneath the diamond surface with concentration of about 0.6 ppm (substrate density of 3.52 g/cm³ and displacement energy of 37.5 eV^{51,52}). The diamond was cut from a diamond chip measuring 2.5 mm × 2.5 mm × 0.3 mm into a diamond beam measuring 2.5 mm × 0.1 mm × 0.1 mm by Syntek Co., Ltd.

Measurement setup

Optical measurements were conducted under an ambient environment using an in-house scanning confocal microscope. Optical excitation was performed using a 532 nm laser (MGL-III-532-20mW Changchun New Industries Optoelectronics Technology Co., Ltd.) focused onto an acousto-optical modulator (AOM) (Isomet 1250C) to provide a controlled pulse excitation with 1 mW of incident power at the sample. The laser was guided through optical lines to a 50 ×, NA = 0.6 objective lens (Nikon TU Plan ELWD). The emitted PL was filtered using a high-pass filter (Semrock BLP01-635R-25) before it was focused and coupled with a single-mode optical fiber and conveyed to a single photon counter module (SPCM) (Perkin Elmer SCPM-ARQH-14FC). The PL

was integrated over a duration of 250 ns. Laser spot positioning on the sample and PL imaging were performed via three-axis piezo nanositioning (MCL nano-LP 100).

A microwave generator (DS Instruments SG6000F) was used to provide microwaves to excite the MSSWs delivered to the diamond. A high-speed multichannel pulse generator (SpinCore Pulse Blaster PBESR-PRO-500) provided transistor–transistor logic signals to the AOM, RF switch (Minicircuit ZYSWA-2-50DR), and SPCM counter gate. A pair of electromagnets was used to provide an in-plane external magnetic field to split the NV spin degeneracy and magnetize the YIG.

To create a temperature gradient in the YIG, two Peltier modules (European Thermodynamics Limited ET-007-05-15) were used in the experiment. Each Peltier module was sandwiched between two aluminum plates; the bottom side of the Peltier modules was thermally connected to a large plate of room-temperature bath, and the upper side of the Peltier modules were thermally connected to hot/cold plates on which the YIG was bridged along the gap of 1 mm. The temperatures of both plates were measured using two T-type thermocouples connected to a dual-channel nanovoltmeter (Keithley 2182A), which provided feedback signals to control two source-meter instruments (ADCMT 6240A) that fed the Peltier modules. A proportional-integral-

derivative control algorithm was applied to control the temperature difference between both ends of the YIG.

Acknowledgments

We thank Eisuke Abe at RIKEN for the fruitful discussions. This study was supported in part by JSPS KAKENHI (JP18H01868, 18H04289, and 19K15444), Japan, by JST CREST (JPMJCR1875 and JPMJCR17I1), and by JST A-STEP (JPMJTM19AV), Japan. N.M. acknowledges support from KAKENHI (15H05868), MEXT Q-LEAP (JPMXS0118067395), Japan.

Author contributions

D.P. and T.A. conceived the experimental idea. D.P. designed and performed the experiments with support from Y.K. and K.H. K.U. provided the YIG sample. D.P., N.M., and T.A. analyzed and discussed the data. D.P. and T.A. wrote the manuscript. All authors discussed the experimental results and commented on the manuscript.

Competing financial interests

The authors declare no competing financial interests.

References

1. Chumak, A. V., Vasyuchka, V. I., Serga, A. A. & Hillebrands, B. Magnon spintronics. *Nature Phys.* **11**, 453-461 (2015).
2. Kajiwara, Y. et al. Transmission of electrical signals by spin-wave interconversion in a magnetic insulator. *Nature* **464**, 262-266 (2010).
3. Cornelissen, L. J., Liu, J., Youssef, J. B. & van Wees, B. J. Long-distance transport of magnon spin information in a magnetic insulator at room temperature. *Nature Phys.* **11**, 1022-1026 (2015).
4. Giles, B. L., Yang, Z., Jamison, J. S. & Myers, R. C. Long-range pure magnon spin diffusion observed in a nonlocal spin-Seebeck geometry. *Phys. Rev. B* **92**, 224415 (2015).
5. Bauer, G. E. W., Saitoh, E. & van Wees, B. J. Spin caloritronics. *Nature Mater.* **11**, 391-399 (2012).
6. Cornelissen, L. J., Liu, J., van Wees, B. J. & Duine, R. A. Spin-current-controlled modulation of the magnon spin conductance in a three-terminal magnon transistor. *Phys. Rev. Lett.* **120**, 097702 (2018).
7. Wu, H. et al. Magnon valve effect between two magnetic insulators. *Phys. Rev. Lett.* **120**, 097205 (2018).
8. Uchida, K. et al. Observation of longitudinal spin-Seebeck effect in magnetic insulators. *Appl. Phys. Lett.* **97**, 172505 (2010).
9. Herbschleb, E. D. et al. Ultra-long coherence times amongst room-temperature solid-state spins, *Nature Commun.* **10**, 3766 (2019)
10. Abe, E. & Sasaki, K. Tutorial: Magnetic resonance with nitrogen-vacancy centers in diamond—microwave engineering, materials science, and magnetometry. *J. Appl. Phys.* **123**, 161101 (2018).
11. Casola, F., van der Sar, T. & Yacoby, A. Probing condensed matter physics with magnetometry based on nitrogen-vacancy centers in diamond. *Nature Rev. Mater.* **3**, 17088 (2018).

12. van der Sar, T., Casola, F., Walsworth, R. & Yacoby, A. Nanometre-scale probing of spin waves using single electron spins. *Nature Commun.* **6**, 7886 (2015).
13. Wolfe, C. S. et al. Off-resonance manipulation of spins in diamond via precessing magnetization of a proximal ferromagnet. *Phys. Rev. B* **89**, 180406(R) (2014).
14. Wolfe, C. S. et al. Spatially resolved detection of complex ferromagnet dynamics using optically detected nitrogen-vacancy spins. *Appl. Phys. Lett.* **108**, 232409 (2016).
15. Andrich, P. et al. Long-range spin wave mediated control of defect qubits in nanodiamonds. *Npj Quantum Inf.* **3**, 28 (2017).
16. Kikuchi, D. et al. Long-distance excitation of nitrogen-vacancy centers in diamond via surface spin waves. *Appl. Phys. Express* **10**, 103004 (2017).
17. Zhou, T. X. et al. A magnon scattering platform. Preprint at <https://arxiv.org/abs/2004.07763> (2020).
18. Bertelli, I. et al. Magnetic resonance imaging of spin-wave transport and interference in a magnetic insulator. Preprint at <https://arxiv.org/abs/2004.07746> (2020).
19. Bender, S. A. & Tserkovnyak, Y. Thermally driven spin torques in layered magnetic insulators. *Phys. Rev. B* **93**, 064418 (2016).
20. Flebus, B., Upadhyaya, P., Duine, R. A. & Tserkovnyak, Y. Local thermomagnonic torques in two-fluid spin dynamics. *Phys. Rev. B* **94**, 214428 (2016).
21. Liu, L., Sun, Y., Jantz, M. & Wu, M. Control of ferromagnetic relaxation in magnetic thin films through thermally induced interfacial spin transfer. *Phys. Rev. Lett.* **108**, 257202 (2012).
22. Kajiwara, Y. et al. Spin-relaxation modulation and spin-pumping control by transverse spin-wave spin current in $Y_3Fe_5O_{12}$. *Appl. Phys. Lett.* **103**, 052404 (2013).
23. Jungfleisch, M. B. et al. Heat-induced damping modification in yttrium iron garnet/platinum hetero-structures. *Appl. Phys. Lett.* **102**, 062417 (2013).

24. Yu, H. et al. Thermal spin torques in magnetic insulators. *Phys. Rev. B* **95**, 104432 (2017).
25. Du, C. et al. Control and local measurement of the spin chemical potential in a magnetic insulator. *Science* **357**, 195-198 (2017).
26. Labanowski, D. et al. Voltage-driven, local, and efficient excitation of nitrogen-vacancy centers in diamond. *Science Adv.* **4**, (2018).
27. Purser, C. M. et al. Spin wave detection by nitrogen-vacancy centers in diamond as a function of probe-sample separation. *Appl. Phys. Lett.* **116**, 202401 (2020).
28. Liu, J. et al. Microwave control of thermal-magnon spin transport. *Phys. Rev. B* **99**, 054420 (2019).
29. Solyom, A. et al. Probing a spin transfer controlled magnetic nanowire with a single nitrogen-vacancy spin in bulk diamond. *Nano Lett.* **18**, 6494-6499 (2018).
30. Wang, X. et al. Electrical control of coherent spin rotation of a single-spin qubit. Preprint at <https://arxiv.org/abs/2007.07543> (2020).
31. Acosta, V. M. et al. Temperature dependence of the nitrogen-vacancy magnetic resonance in diamond. *Phys. Rev. Lett.* **104**, 070801 (2010).
32. Toyli, D. M. et al. Measurement and Control of Single Nitrogen-Vacancy Center Spins above 600 K. *Phys. Rev. X* **2**, 031001 (2012).
33. Eshbach, J. R. & Damon, R. W. Surface magnetostatic modes and surface spin waves. *Phys. Rev.* **118**, 1208 (1960).
34. Mühlherr, C., Shkolnikov, V. O. & Burkard, G. Magnetic resonance in defect spins mediated by spin waves. *Phys. Rev. B* **99**, 195413 (2019).
35. Dreau, A. et al. Avoiding power broadening in optically detected magnetic resonance of single NV defects for enhanced dc magnetic field sensitivity. *Phys. Rev. B* **84**, 195204 (2011).
36. Wang, P. et al. High-resolution vector microwave magnetometry based on solid-state spins in diamond. *Nature Commun.* **6**, 6631 (2015).

37. Hanson, R., Dobrovitski, V. V., Feiguin, A. E., Gywat, O. & Awschalom, D. D. Coherent dynamics of a single spin interacting with an adjustable spin bath. *Science* **320**, 352-355 (2008).
38. An, T. et al. Unidirectional spin-wave heat conveyer. *Nature Mater.* **12**, 549-553 (2013).
39. Wong, K. L. et al. Unidirectional propagation of magnetostatic surface spin waves at a magnetic film surface. *Appl. Phys. Lett.* **105**, 232403 (2014).
40. Giles, B. L. et al. Thermally driven long-range spin currents in yttrium iron garnet due to intrinsic spin Seebeck effect. *Phys. Rev. B* **96**, 180412 (2017).
41. Shan, J. et al. Criteria for accurate determination of the magnon relaxation length from the nonlocal spin Seebeck effect. *Phys. Rev. B* **96**, 184427 (2017).
42. Guan, Y., Bailey, W. E., Vescovo, E., Kao, C. -C. & Arena, D. A. Phase and amplitude of element-specific moment precession in Ni₈₁Fe₁₉. *J. Magn. Magn. Mater.* **312**, 374-378 (2007).
43. Pozar, D. M. *Microwave Engineering* (John Wiley & Sons, Hoboken, 1998).
44. Page, M. R. et al. Optically detected ferromagnetic resonance in diverse ferromagnets via nitrogen vacancy centers in diamond. *J. Appl. Phys.* **126**, 124902 (2019).
45. Lee-Wong, E. et al. Nanoscale detection of magnon excitations with variable wavevectors through a quantum spin sensor. *Nano Lett.* **20**, 3284-3290 (2020).
46. Schwabl, F. *Advanced Quantum Mechanics* (Springer, Berlin, 2005).
47. Tetienne, J.-P. et al. Spin relaxometry of single nitrogen-vacancy defects in diamond nanocrystals for magnetic noise sensing. *Phys. Rev. B* **87**, 235436 (2013).
48. Wrachtrup, J. & Finkler, A. Single spin magnetic resonance. *J. Magn. Reson.* **269**, 225–236 (2016).
49. Kurizki, G. et al. Quantum technologies with hybrid system. *Proc. Natl. Acad. Sci.* **112**, 3866-3873 (2015).

50. Ziegler, J. F. *The stopping and ranges of ions in matter*, <http://www.srim.org>.
51. Toyli, D. M., Weis, C. D., Fuchs, G. D., Schenkel, T. & Awschalom, D. D. Chip-scale nanofabrication of single spins and spin arrays in diamond. *Nano Lett.* **10**, 3168 (2010).
52. Koike, J., Parkin, D. M. & Mitchell, T. E. Displacement threshold energy for type IIa diamond. *Appl. Phys. Lett.* **60**, 1450 (1992).